Front. Mech. Eng.
https://doi.org/10.1007/s11465-018-0488-8

RESEARCH ARTICLE

Zheng-Dong MA

Macro-architectured cellular materials: Properties, characteristic modes, and prediction methods

Abstract Macro-architectured cellular (MAC) material is defined as a class of engineered materials having configurable cells of relatively large (i.e., visible) size that can be architecturally designed to achieve various desired material properties. Two types of novel MAC materials, negative Poisson's ratio material and biomimetic tendon reinforced material, were introduced in this study. To estimate the effective material properties for structural analyses and to optimally design such materials, a set of suitable homogenization methods was developed that provided an effective means for the multiscale modeling of MAC materials. First, a strain-based homogenization method was developed using an approach that separated the strain field into a homogenized strain field and a strain variation field in the local cellular domain superposed on the homogenized strain field. The principle of virtual displacements for the relationship between the strain variation field and the homogenized strain field was then used to condense the strain variation field onto the homogenized strain field. The new method was then extended to a stress-based homogenization process based on the principle of virtual forces and further applied to address the discrete systems represented by the beam or frame structures of the aforementioned MAC materials. The characteristic modes and the stress recovery process used to predict the stress distribution inside the cellular domain and thus determine the material strengths and failures at the local level are also discussed.

Keywords architectured material, cellular materials, multi-scale modeling, homogenization method, effective material properties, computational method

Received May 7, 2017; accepted August 14, 2017

Zheng-Dong MA (✉)
The University of Michigan, Ann Arbor, MI 48109, USA
E-mail: mazd@umich.edu

1 Introduction

1.1 Tendency of the new material development

Lightweight materials have become a critical requirement for reducing the weight of automotive and aerospace vehicles to achieve better fuel efficiency, lower emissions, and improved environmental protection. Parallel to the effort of improving the strength of traditional metal materials, new materials, such as fiber-reinforced composites, foams, lattice, and sandwich materials have been developed to expand the boundaries of the material property space defined by traditional solid materials. Important features in these new materials include 1) using two or more raw materials in a composition to form a new material, and 2) introducing porosity into solid materials. The use of two or more raw materials in a composite makes it possible to make the best use of the unique properties of raw materials and to compensate for their weaknesses. For example, fiber materials usually have very high tension strength but have no compression resistance. By composting fiber materials, e.g., carbon fiber with a matrix material such as resin, the weakness of the fiber can be overcome. However, introducing porosity in a composite material usually can further improve the bending stiffness (and other features) of the resulting structure and reduce the weight significantly. These new materials are artificially made and usually have a cellular structure with some kind of architecture within the characteristic cells; therefore, they are called "architectured cellular materials" in this study [1].

In our opinion, there are two opposite tendencies in the development of architectured materials: One tendency is to reduce the scale of the materials, i.e., by having smaller cells, and the other is increase it. Nowadays, researchers have been able to fabricate new materials in very small scales, such as nano and atomic scales. As shown on the left side of Fig. 1, graphene, nanotube, and micro-trusses have been developed. These kinds of materials are called micro-architectured materials [2]. Even though micro-

architectured materials can achieve an extra-high strength/weight ratio, they can usually only be used as reinforcement in a matrix material if their structural functionalities are to be utilized. However, architectured materials can be fabricated in a larger scale with relatively larger cells as shown on the right side of Fig. 1. We call the architectured materials with larger cells "macro-architectured cellular" (MAC) materials, which usually can provide a better structure performance/cost ratio [3,4] and can easily expand the coverage of the material property space [1].

1.2 Macro-architectured cellular (MAC) materials

MAC material is defined as a class of engineered materials that has configurable cells in a relatively larger size (compared with micro-architectured materials [2]). MAC materials can be designed to suit various desired material properties. Figure 2 illustrates a roadmap of MAC material development. As shown in Figure 2, first, solid materials are fabricated as architectured structures for improving the efficiency of the material usage in the structures. For example, I-beams and channel strips are developed to have special cross-section shapes to achieve better load-bearing capability with less weight. Next, two or multiple materials are synthesized to form various composite materials such as carbon-fiber-reinforced polymer composites with typical woven configurations of fibers. Finally, porosities are introduced into the materials with various cellular configurations to treat empty space with the functionality of the materials, which is a major feature of MAC materials. Figure 2 also illustrates that the use of multiple raw materials (including a single material) with an architectured cellular design of the unit cell make it possible to obtain high-performance, function-oriented, and low-cost materials. In contract to micro-architectured cellular materials, MAC materials can be manufactured with combined traditional fabrication techniques, such as metal cutting, stamping, welding, bolding, gluing, molding, weaving, and braiding, which results in better productivity.

Figure 3 shows some examples of MAC materials found on the Internet. Figure 3 illustrates that MAC materials can be fabricated using various manufacturing methods, including material penetration, material expanding, weaving, foaming, 3D weaving, and stamping + welding. Figure 4 shows further examples of MAC materials being fabricated using a 3D printing machine, which illustrates that modern additive manufacturing technologies have opened the door for producing a variety of novel MAC materials which have never before seemed possible. Two novel types of MAC material have recently been developed by this author's research group, namely negative Poisson's ratio (NPR) materials [5] and biomimetic tendon reinforced (BTR) materials [6,7], which will be introduced in Section 2.

The characteristics and general features of MAC materials can be summarized as follows:

1) The creation of a MAC involves the removal of the low-efficiency portion of a material;

2) It involves the addition of porosity into a solid material;

3) MAC materials are created by using two or more raw materials if possible;

4) They are architecturally designed;

5) Function-oriented design is employed in developing them;

6) This enables maximization of the multi-functionality of material;

7) They can be manufactured using traditional fabrication techniques, e.g., metal cutting, stamping, welding, bonding, gluing, molding, weaving, and braiding;

8) They may be effectively developed using 3D printing.

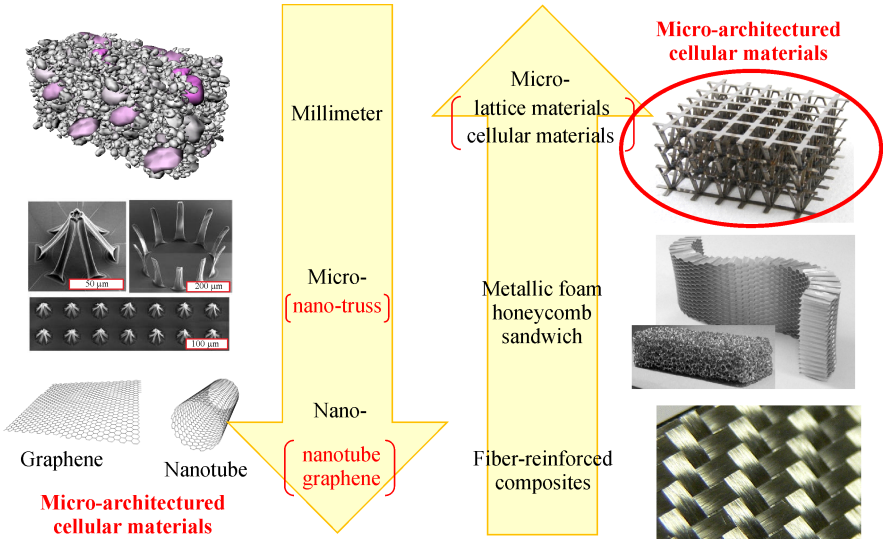

Fig. 1 Tendency of new material development. Left: Going to a smaller scale; right: Going to a larger scale

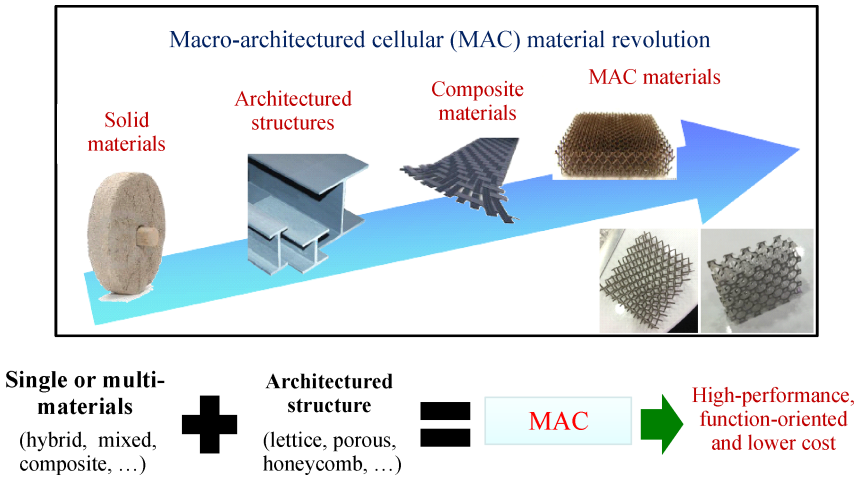

Fig. 2 Roadmap of MAC materials

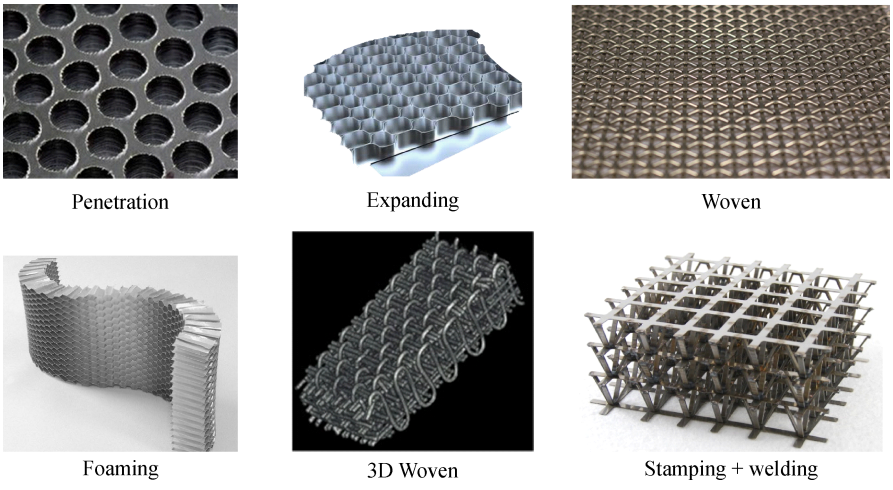

Fig. 3 Example MAC materials

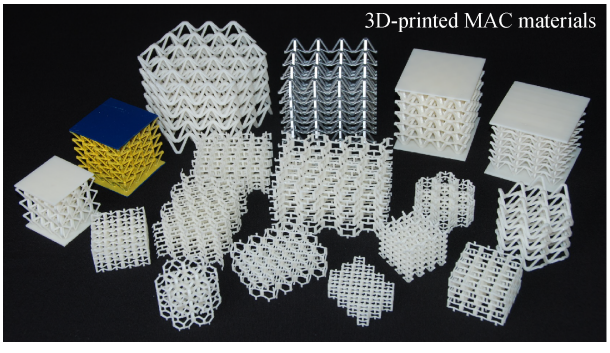

Fig. 4 MAC materials by 3D printing (fabricated at MKP Structural Design Associates, Inc.)

1.3 Prediction methods of effective material properties of MAC materials

Multiscale modeling and homogenization have become rich areas of research. Fruitful results have been published with a wide range of applications as listed in recent literature review papers [8−10]. Homogenization, especially asymptotic homogenization [11−13], provides a powerful mathematical tool for bridging different scale modeling problems and solving micro-macro, local-global, nano-macro, multiscale modeling problems. The applicable areas include so-called heterogeneous materials, cellular materials, granular materials, and fiber-reinforced polymers. The homogenization method has also been utilized in topology optimization processes [14,15]. Although the advantages in the mathematical process of asymptotic homogenization are appreciated, they are often overlooked in favor of the "mechanics logics" inside the homogenization modeling process. Existing asymptotic homogenization methods [16−20] have provided effective means for the multiscale modeling of continuum solids; however, there is a need for extending them to more general applications such as handling the discrete systems

discussed in this study. To estimate the effective material properties and to optimally design the MAC materials discussed in this study, a more suitable homogenization process is needed.

This study provides a new homogenization process that is based on engineering and mechanics rather than on mathematics. It is useful to provide a more systematic explanation for mechanics-based homogenization. Another important point is that, theoretically, the mathematical asymptotic homogenization process requires a micro-cell to be small or infinitely small to assume convergence of the process, but this is not necessary for mechanics-based homogenization. In fact, mechanics-based homogenization can be considered a coordinate reduction process like a Guyan reduction [21], which is widely used in solving structural dynamics problems. Therefore, relatively larger size cells can be treated in various applications, including in architectured cellular materials.

First, continuum solids were considered and a mechanics-based homogenization process was developed based on the principle of virtual displacements. Mechanics-based homogenization provides a better understanding in terms of the mechanics behind the homogenization process. This new approach separates the strain field into a homogenized strain field along with a strain variation field in the local cellular domain superposed on the homogenized strain field. The principle of virtual displacements describing the relationship between the strain variation field and the homogenized strain field is then used to condense the strain variation field to the homogenized strain field. Hence, the homogenization process is treated as a coordinate reduction process like a Guyan reduction.

The new method has two variants: One is a strain-based homogenization, and the other is a stress-based homogenization. The stress-based homogenization process is obtained based on the principle of virtual forces. Similar to strain-based homogenization, stress-based homogenization separates the stress field into a homogenized stress field and a stress variation field superposed on the homogenized stress field. The principle of virtual forces is then used to condense the stress variation field into the homogenized stress field. The stress-based homogenization process can be extended easily to address discrete systems, such as those MAC materials modeled by beam and frame structures. The new method is then utilized to obtain the effective material properties of the MAC materials discussed in this study.

New formulas were obtained to calculate the effective mass density and body forces with improved approximations, which can be further extended to consider other body forces such as thermal and magnetic forces. The characteristic strain modes and corresponding characteristic displacement modes are discussed. A recovery process is further considered for recovering the local strain and stress in the cellular domain after the global analysis.

2 Two novel MAC materials

Two types of useful MAC materials have been developed [5−7]. One type is the three-dimensional NPR material [5] shown in Fig. 5, and the other is the so-called BTR material [6−7]. Both are originally obtained through the topology optimization process developed in Ref. [14]. These new materials are similar to traditional lattice materials, but they can be made of multiple raw materials and cannot be

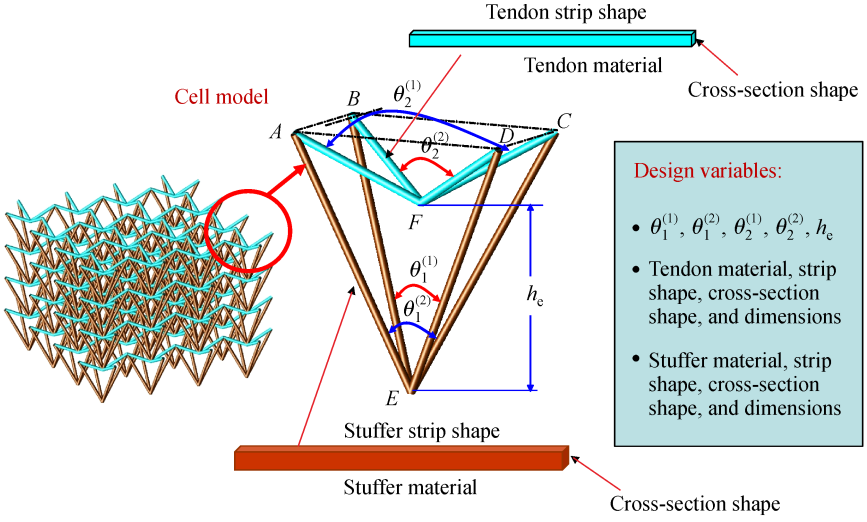

Fig. 5 Design variables in a 3D NPR material cell

referred to as “micro” because of their relatively larger size.

2.1 NPR materials

Figure 5 illustrates the material cell model for the three-dimensional NPR materials invented in Ref. [5]. NPR materials are also called auxetic, anti-rubber, and dilatational materials. Since Lakes [22] published his article in *Science* in 1987, NPR materials have attracted increasingly more attention because of their unique behavior. Unlike conventional materials, NPR materials may shrink when compressed and expand when stretched along the perpendicular direction. The unique features of NPR materials include, but are not limited to, stiffening under a load, impact energy absorption, and the ability to be engineered to have other desired functionalities.

As shown in Fig. 5, the invented NPR structure comprises a pyramid-shaped unit cell having four base points, A, B, C, and D defining the corners of a square lying in a horizontal plane. Four stuffers of equal length or different lengths extend from one of the respective base points to a Point E spaced apart from the plane. Four tendons of equal length or different lengths, but less than the lengths of the stuffers, extend from one of the base points to Point F between Point E and the plane. There are, in general, five parameters that determine the cell geometry, i.e., $\theta_1^{(1)}$, $\theta_1^{(2)}$, $\theta_2^{(1)}$, $\theta_2^{(2)}$, and h_e. For simplicity, in this study, we assumed $\theta_1^{(1)} = \theta_1^{(2)} = \theta_1$ and $\theta_2^{(1)} = \theta_2^{(2)} = \theta_2$, such that the geometrical parameters were reduced to three: θ_1, θ_2, and h_e. The design parameters of the NPR cell include the material properties of the stuffers and tendons, as well as the shapes of the strips and the cross-section shapes of the stuffers and tendons. In this study, we assumed that the strips were straight and had constant cross-sectional shapes that can be represented by E_1, A_1, I_1, and ρ_1 for the stuffers and E_2, A_2, I_2, and ρ_2 for the tendons. Note, however, the strips can be curved and the cross-section shapes can be varied along the axial line.

In the three-dimensional configurations, a collection of unit cells was arranged as tiles in the same horizontal plane with the base points of each cell connected to the base points of the adjoining cells, thereby forming a horizontal layer. A collection of horizontal layers was then stacked with each point E of the cells in one horizontal layer being connected to Point F of the cells in the adjacent layer. The above facts can be used to determine the connectivity among the adjacent cells and then used to determine the boundary conditions for the cell analyses in the homogenization process.

As shown in Fig. 6, special properties of the NPR materials include a) a reaction to a load (stiffening under pressure), b) a wide range of material property coverage, c) the ability to be functionally graded and function-oriented designed, and d) an excellent impact energy absorption capability for lightweight anti-collision energy absorption structures. Figure 6(a) illustrates that a MAC material with

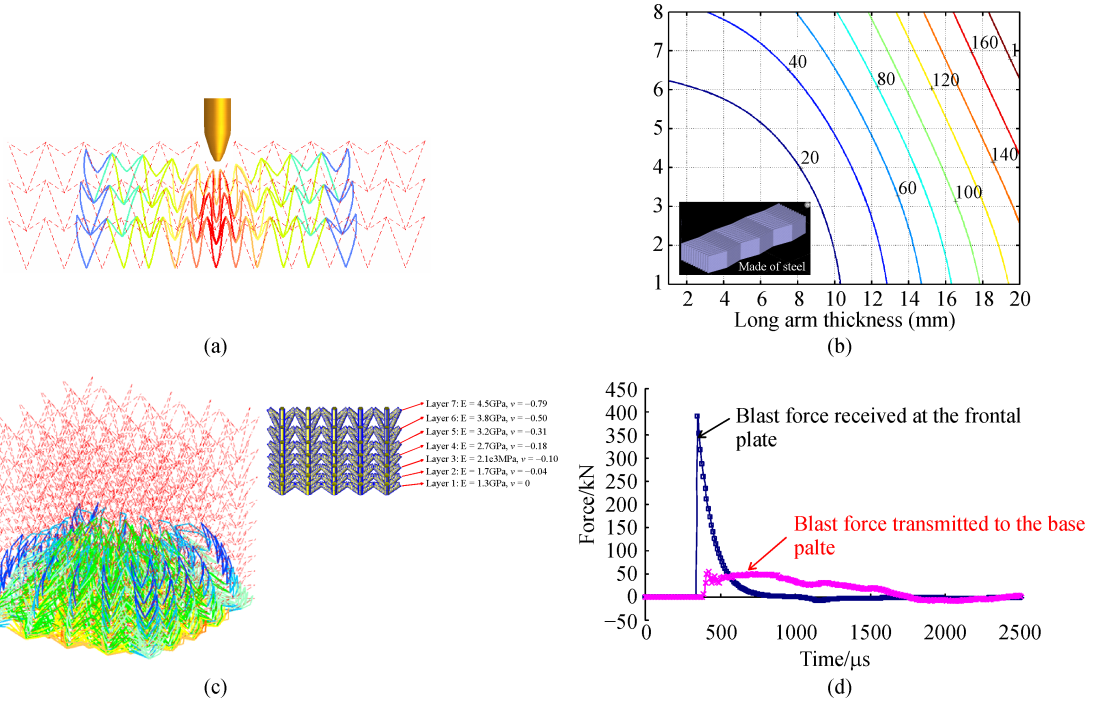

Fig. 6 Special properties of NPR materials. (a) Reaction to load (stiffening under pressure); (b) wide range of material property coverage; (c) able to be functionally graded and function-oriented designed; (d) excellent impact energy absorption capability

NPR properties was shrinking under a concentrated load, thus providing more resistance to the load. Figure 6(b) illustrates that a quasi-3D metallic NPR material can cover a wide range of Yong's modulus by varying only two angular design variables defined in Figure 5. Figure 6(c) illustrates that the layer-by-layer design of a 3D NPR material can deform to a special shape under a blast load that can deflect the blast wave. Figure 6(d) further illustrates a blast testing result, which shows a significant blast impact force was insulated by the NPR material.

Potential applications of NPR materials include, but are not limited to:

- Lightweight anti-collision energy absorption components such as bushings, bumpers, and mounts [23];
- Non-pneumatic tires [24];
- Anti-explosion energy-absorption materials;
- Deployable structures [25];
- New types of sofa cushions and mattresses, and
- Stents [26].

2.2 BTR materials

Figure 7 illustrates the parameterization of the BTR materials proposed in literature [6,7]. As shown in Fig. 7, BTR has three major components: 1) Cover sheets on the top and bottom, which are usually made of thin composites (such as fiber-reinforced polymer) or metallic sheets, 2) stuffers, which are usually made of stiff materials such as metallic columns, ceramics, or high-stiffness composites, and 3) tendons, which are usually made of high-strength tension materials, such as metal wires or high-strength fibers. In summary, BTR materials can be made of various raw materials depending on the application. Major features of BTR materials are their lightweight and high material efficiencies, especially their out-of-plane bending stiffness as compared to existing composite materials. As shown in Fig. 7, the major design parameters for the geometry of BTR materials are h_2, l_1, and t_1. Other design parameters include the material properties of sheets, stuffers, and tendons represented by E_i and ρ_i $(i = 1,2,3)$, the cross-sectional area of the stuffers represented by A_2, and the cross-sectional area of the tendons, A_3.

Potential applications of BTR materials include, but are not limited to:

- Lightweight anti-collision components such as bumpers of automotive vehicles;
- Covering panels for vehicle body structures;
- Lightweight anti-explosion protection materials, e.g., armor [27,28] and battery protection boxes;
- Building materials, insulation walls, roofs, and solar panels;
- Lightweight furniture, desks, doors, and dividing panels; and
- Mobile homes and template building with high strength and improved thermal protection.

3 MAC material property prediction methods

Existing asymptotic homogenization methods [11−13] have provided effective means for the multiscale modeling of continuum solids; however, they are often overlooked in favor of the "mechanics logics" inside the homogenization modeling process, and there is a need for extending them to more general applications such as handling the discrete systems discussed in this study. This study provides a mechanics-based homogenization method based on engineering and mechanics rather than on mathematics. First, a mechanics-based homogenization process was developed based on the principle of virtual displacements. The new approach separates the strain field into a homogenized strain field along with a strain variation field in the local cellular domain superposed on the homogenized strain field. The principle of virtual displacements describing the

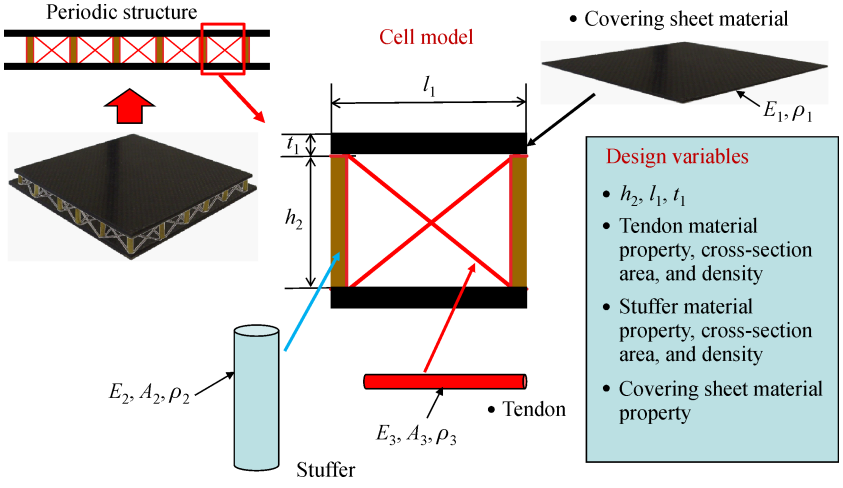

Fig. 7 Design variables in a BTR material cell

relationship between the strain variation field and the homogenized strain field was then used to condense the strain variation field to the homogenized strain field. Hence, the homogenization process was treated as a coordinate reduction process.

3.1 Governing equation

The elastostatics problem of a MAC material cell can be defined in a form of principle of virtual displacements with an extension to an elastic-dynamics problem as shown in Eq. (1). Here Ω_ε ($\Omega_\varepsilon \subset R^3$) was assumed to be a structural domain with a cellular structure that is in periodic or other forms, provided the proper connections among the adjacent cells can be defined; Γ_t is the traction boundary of Ω_ε.

$$\int_{\Omega_\varepsilon} \delta\boldsymbol{\varepsilon}^{\mathrm{T}}\mathbf{D}^{\varepsilon}\boldsymbol{\varepsilon}\mathrm{d}\Omega + \int_{\Omega_\varepsilon} \delta\boldsymbol{u}^{\mathrm{T}}\rho^{\varepsilon}\ddot{\boldsymbol{u}}\mathrm{d}\Omega = \int_{\Omega_\varepsilon} \delta\boldsymbol{u}^{\mathrm{T}}\boldsymbol{f}^{\varepsilon}\mathrm{d}\Omega + \int_{\Gamma_t} \delta\boldsymbol{u}^{\mathrm{T}}\mathbf{t}\mathrm{d}\Gamma_t, \tag{1}$$

where $\boldsymbol{\varepsilon}$ denotes the engineering strain vector ($\boldsymbol{\varepsilon}^{\mathrm{T}} = \{\varepsilon_x,\varepsilon_y,\varepsilon_z,\gamma_{yz},\gamma_{zx},\gamma_{xy}\}^{\mathrm{T}}$), $\boldsymbol{u}$ denotes the displacement vector, $\ddot{\boldsymbol{u}} = \partial^2\boldsymbol{u}/\partial t^2$ denotes the acceleration vector, $\boldsymbol{f}^{\varepsilon}$ denotes the body force vector, and $\boldsymbol{t}$ is the boundary traction vector, $\delta\boldsymbol{\varepsilon}$ denotes the virtual strain vector, $\delta\boldsymbol{u}$ denotes the virtual displacement vector, $V = \{\delta\boldsymbol{u} \in H^1(\Omega_\varepsilon)|\delta\boldsymbol{u}|_{\Gamma_d} = 0\}$ denotes the space of kinematically admissible displacement fields, and Γ_d is the displacement boundary. $H^1(\Omega_s)$ is the Sobolev space in which the strain energy of the structure is finite. $\boldsymbol{D}^{\varepsilon}$ denotes the elasticity matrix before the homogenization, and ρ^{ε} is the density before the homogenization.

For simplicity, in the following, we assume a three-dimensional solids problem, even though the formulation obtained can be applied to two-dimensional solids problems and problems such as beams, plates, or shells. We also assume a linear elasticity problem with a constitute law $\boldsymbol{\sigma} = \boldsymbol{D}\boldsymbol{\varepsilon}$, where $\boldsymbol{\sigma}$ is a Cauchy stress vector ($\boldsymbol{\sigma}^{\mathrm{T}} = \{\sigma_x,\sigma_y,\sigma_z,\tau_{yz},\tau_{zx},\tau_{xy}\}^{\mathrm{T}}$), and $\boldsymbol{D} = [\boldsymbol{D}_{ij}]_{6\times6}$ is the material stiffness matrix, even though the formulation obtained can be extended easily to nonlinear problems.

Note, the principle of virtual displacements requires the following continuity conditions to be satisfied:

$$\varepsilon = \boldsymbol{E}(\nabla)\boldsymbol{u}\ ,\delta\varepsilon = \boldsymbol{E}(\nabla)\delta\boldsymbol{u}, \tag{2}$$

where

$$\boldsymbol{E}(\nabla) = \begin{bmatrix} \frac{\partial}{\partial x} & 0 & 0 & 0 & \frac{\partial}{\partial z} & \frac{\partial}{\partial y} \\ 0 & \frac{\partial}{\partial y} & 0 & \frac{\partial}{\partial z} & 0 & \frac{\partial}{\partial x} \\ 0 & 0 & \frac{\partial}{\partial z} & \frac{\partial}{\partial y} & \frac{\partial}{\partial x} & 0 \end{bmatrix}^{\mathrm{T}}. \tag{3}$$

3.2 Material property calculation method-homogenization process

The asymptotic homogenization method (AHM) [11−13] for an elastostatic continuum was derived using the mathematical approach described below. First, it was assumed that the structure in a domain Ω_ε had a Y-periodic microstructure. The periodicity is represented by a parameter ε, which is very small, and the elastic tensor is given in the form of $E^{\varepsilon}_{ijkl} = E_{ijkl}(x, y)$ where $y \rightarrow E_{ijkl}(x,y)$ is the Y-periodic, x is the macroscopic variation of the material parameters, and $y = x/\varepsilon$ gives the microscopic periodic variations. Supposing that the structure is subjected to a macroscopic body force and a macroscopic surface traction, the resulting displacement field $u^{\varepsilon}(x)$ can then be expanded as $u^{\varepsilon}(x) = u_0(x) + \varepsilon u_1(x, y) + o(\varepsilon^2)$ where the leading term $u_0(x)$ is a macroscopic deformation field that is independent of the microscopic variable and $u_1(x, y)$ is a microscopic deformation field. Substituting the above assumptions into the governing equation and comparing the terms in the same order of ε, one can obtain the effective material properties (i.e., Eq. (15)) and the homogenized governing equation (i.e., Eq. (14)) [1].

Note that the aforementioned AHM approach was obtained based on the assumption of infinitely small cellular cells; however, it does not explain why, in many cases, one cannot obtain better results by considering higher-order terms of ε, which indicates that the Taylor expansion in the approach may not generally converge. The approach also has a theoretical limitation in its extension to larger cells. It lacks explicit instructions for how to determine the boundary conditions in a micro-cell analysis with the exception of mentioning the use of the periodic boundary conditions. In fact, the periodic boundary conditions may not be able to remove the rigid body motion of the micro-cell, and different boundary conditions may be required to solve different subcases in the homogenization process, as illustrated in Section 3.6.

It is important to provide a more systematic explanation for the homogenization process. Another important point is that, theoretically, the mathematical asymptotic homogenization process requires the micro-cell to be small or infinitely small to assume convergence of the process, but this is not necessary for mechanics-based homogenization. In fact, mechanics-based homogenization can be considered a coordinate reduction process like a Guyan reduction [21], which is widely used in solving structural dynamics problems. Therefore, relatively large-size cells can be treated in various applications, including in architectured cellular materials.

We employed an approach based on an engineering approach and the mechanics of the problem. We considered mechanics-based homogenization as a coordinate reduction process analogous to the Guyan reduction described in Ref. [1]. Unlike the AHM approach, we

considered a macro-structural problem with the same coordinate system describing both the homogenized (global) problem and the local problem in the cellular domain Y. Then, the strain in the domain Y could be calculated by the same differential operator as that of the global strain. However, it was assumed in this study that 1) the cellular structure had periodic cells (even the periodicity can change from place to place provided the connectivity is assured), 2) the dimensions of the cells were considerably small compared with the dimensions of the structure, and 3) the material sample was taken from a large portion of the structure, so that structure's boundary effects on the homogenization process could be ignored.

Instead of separating the nodal coordinates into internal coordinates and boundary coordinates as in a Guyan reduction, we separated the strain field $\boldsymbol{\varepsilon}$ into a homogenized strain field $\boldsymbol{\varepsilon}_{\mathrm{h}}$ that is constant over the cellular domain and continuous over the homogenized structural domain, and a strain variation field $\boldsymbol{\varepsilon}_{\mathrm{v}} = \boldsymbol{\varepsilon}_{\mathrm{v}}(y)$ ($y \in Y$) superposed on $\boldsymbol{\varepsilon}_{\mathrm{h}}$, which is defined in the cellular Y domain and varies in Y, to obtain

$$\boldsymbol{\varepsilon} = \boldsymbol{\varepsilon}_{\mathrm{h}} + \boldsymbol{\varepsilon}_{\mathrm{v}}. \tag{4}$$

The displacement fields corresponding to $\boldsymbol{\varepsilon}_h$ and $\boldsymbol{\varepsilon}_v$ are denoted as $\boldsymbol{u}_h$ and $\boldsymbol{u}_v$, and we get

$$\boldsymbol{u} = \boldsymbol{u}_{\mathrm{h}} + \boldsymbol{u}_{\mathrm{v}}, \tag{5}$$

as well as the following relationships:

$$\boldsymbol{\varepsilon}_{\mathrm{h}} = \boldsymbol{E}(\nabla)\boldsymbol{u}_{\mathrm{h}} \text{ (in } \Omega) \text{ and } \varepsilon_v = \boldsymbol{E}(\nabla)\boldsymbol{u}_{\mathrm{v}} \text{ (in } Y) \ . \tag{6}$$

Substituting Eq. (4) into Eq. (1) produces

$$\int_{\Omega_\varepsilon} (\delta\boldsymbol{\varepsilon}_{\mathrm{h}} + \delta\boldsymbol{\varepsilon}_{\mathrm{v}})^{\mathrm{T}}\boldsymbol{D}^{\varepsilon}(\varepsilon_{\mathrm{h}} + \varepsilon_{\mathrm{v}})\mathrm{d}\Omega + \int_{\Omega_\varepsilon} \delta\boldsymbol{u}^{\mathrm{T}}\rho^{\varepsilon}\ddot{\boldsymbol{u}}\mathrm{d}\Omega$$

$$= \int_{\Omega_\varepsilon} \delta\boldsymbol{u}^{\mathrm{T}}\boldsymbol{f}^{\varepsilon}\mathrm{d}\Omega + \int_{\Gamma_t} \delta\boldsymbol{u}^{\mathrm{T}}\boldsymbol{t}\mathrm{d}\Gamma_{\mathrm{t}}. \tag{7}$$

Equation (7) can be separated as

$$\begin{cases} \displaystyle\int_{\Omega_\varepsilon} \delta\boldsymbol{\varepsilon}_{\mathrm{h}}^{\mathrm{T}}\boldsymbol{D}^{\varepsilon}(\boldsymbol{\varepsilon}_{\mathrm{h}} + \boldsymbol{\varepsilon}_{\mathrm{v}})\mathrm{d}\Omega + \int_{\Omega_\varepsilon} \delta\boldsymbol{u}^{\mathrm{T}}\rho^{\varepsilon}\ddot{\boldsymbol{u}}\mathrm{d}\Omega \\ = \displaystyle\int_{\Omega_\varepsilon} \delta\boldsymbol{u}^{\mathrm{T}}\boldsymbol{f}^{\varepsilon}\mathrm{d}\Omega + \int_{\Gamma_{\mathrm{t}}} \delta\boldsymbol{u}^{\mathrm{T}}\boldsymbol{t}\mathrm{d}\Gamma_{\mathrm{t}} \\ \displaystyle\int_{Y} \delta\boldsymbol{\varepsilon}_{\mathrm{v}}^{\mathrm{T}}\boldsymbol{D}^{\varepsilon}(\boldsymbol{\varepsilon}_{\mathrm{h}} + \boldsymbol{\varepsilon}_{\mathrm{v}})\mathrm{d}y = 0 \quad (\forall Y \subset \Omega_\varepsilon) \end{cases} . \tag{8}$$

Notably, if both equations in Eq. (8) are satisfied while satisfying the continuity conditions in Eq. (6) and the connectivity among adjacent cells, then the original equation, Eq. (7) (i.e., Eq. (1)), will be satisfied. Here, theoretically, we do not have to assume that the cellular Y domain is small. Furthermore, note that periodicity and connectivity together defined boundary conditions among the adjacent cells, and therefore the second equation in Eq. (8) became solvable.

To solve the second equation in Eq. (8), we represent the strain variation $\varepsilon_{\mathrm{v}} = \varepsilon_{\mathrm{v}}(y)$ with a mode superposition technique; whereas, in Eq. (9), $\boldsymbol{\varphi}(y)$ is a matrix constructed of d modes ($d = 6$ for the three-dimensional solids, $d = 3$ for the two-dimensional solids, and d can be other numbers for, e.g., beams, plates, and shells problems) with $\boldsymbol{\varepsilon}_{\mathrm{h}}$ as the modal coordinates, namely

$$\boldsymbol{\varepsilon}_{\mathrm{v}}(y) = \boldsymbol{\varphi}(y)\varepsilon_{\mathrm{h}} \ (y \in Y). \tag{9}$$

Note, Eq. (9) is an equivalent transformation; therefore, there is no error induced as long as the modes in $\boldsymbol{\varphi}$ are linearly independent. Substituting Eq. (9) into the second-row equation in Eq. (8) results in

$$\left[\int_Y \delta\boldsymbol{\varepsilon}_{\mathrm{v}}^{\mathrm{T}}\boldsymbol{D}^{\varepsilon}(\boldsymbol{I} + \boldsymbol{\varphi})\mathrm{d}y\right]\boldsymbol{\varepsilon}_{\mathrm{h}} = 0, \tag{10}$$

or

$$\int_Y \delta\boldsymbol{\varepsilon}_{\mathrm{v}}^{\mathrm{T}}\boldsymbol{D}^{\varepsilon}(\boldsymbol{I} + \boldsymbol{\varphi})\mathrm{d}y = 0. \tag{11}$$

Solving Eq. (11) with the continuity conditions in Eq. (6) and the properly defined boundary conditions (periodic boundary conditions for now), we obtain $\boldsymbol{\varphi}(y)$ ($y \in Y$), and $\boldsymbol{\varepsilon}_{\mathrm{v}}$ now becomes a function of $\boldsymbol{\varepsilon}_{\mathrm{h}}$. We now assume that the displacement field corresponding to $\boldsymbol{\varepsilon}_{\mathrm{v}}$ can be obtained as

$$u_{\mathrm{v}} = \theta(y)u_{\mathrm{h}} \ (y \in Y), \tag{12}$$

where $\boldsymbol{\theta}(y)$ satisfies

$$\boldsymbol{\varphi}(y) = \boldsymbol{E}(\nabla)\boldsymbol{\theta}(y) \ (y \in Y). \tag{13}$$

Then, substituting Eqs. (9) and (12) into the first-row equation in Eq. (8) results in

$$\int_\Omega \delta\boldsymbol{\varepsilon}_{\mathrm{h}}^{\mathrm{T}}\boldsymbol{D}^{H}\boldsymbol{\varepsilon}_{\mathrm{h}}\mathrm{d}\Omega + \int_\Omega \delta\boldsymbol{u}_{\mathrm{h}}^{\mathrm{T}}\rho^{H}\ddot{\boldsymbol{u}}_{\mathrm{h}}\mathrm{d}\Omega$$

$$= \int_\Omega \delta\boldsymbol{u}_{\mathrm{h}}^{\mathrm{T}}\boldsymbol{f}^{H}\mathrm{d}\Omega + \int_{\Gamma_{\mathrm{t}}} \delta\boldsymbol{u}_{\mathrm{h}}^{\mathrm{T}}\boldsymbol{t}^{H}\mathrm{d}\Gamma_{\mathrm{t}}, \tag{14}$$

where Ω stands for the homogenized domain of Ω_ε, and

$$\boldsymbol{D}^{H} = \frac{1}{|Y|}\int_Y \boldsymbol{D}^{\varepsilon}(\boldsymbol{I} + \boldsymbol{\varphi})\mathrm{d}y, \tag{15}$$

$$\boldsymbol{\rho}^{H} = \frac{1}{|Y|}\int_Y \Big(\boldsymbol{I} + \boldsymbol{\theta}(y)\Big)^{\mathrm{T}}\rho^{\varepsilon}\Big(\boldsymbol{I} + \boldsymbol{\theta}(y)\Big)\mathrm{d}y, \tag{16}$$

$$\boldsymbol{f}^{H} = \frac{1}{|Y|}\int_Y \Big(\boldsymbol{I} + \boldsymbol{\theta}(y)\Big)^{\mathrm{T}}\boldsymbol{f}_v^{\varepsilon}\mathrm{d}y, \tag{17}$$

$$\boldsymbol{t}^{H} = \frac{1}{|L|}\int_{\Gamma_{tY}} \Big(\boldsymbol{I} + \boldsymbol{\theta}(y)\Big)^{\mathrm{T}}\boldsymbol{t}\mathrm{d}s, \tag{18}$$

where $\Gamma_{tY} = \Gamma_t \cap Y$.

Notably, the homogenized material stiffness matrix in Eq. (15) is exactly the same what obtained from the asymptotic homogenization method [1]; however, the effective mass density in Eq. (16), the effective internal force in Eq. (17), and the effective traction in Eq. (18) are different from the traditional asymptotic homogenization process. The AHM can only provide averaged mass density, averaged body force, and averaged traction, but the new method gives the material properties from a process like the static condensation, which results in better accuracy for high-frequency analyses problems. Also, note that unlike Guyan reduction, which condenses the internal degree-freedoms into the boundary degree-freedoms, the new method condenses the representatives of the strain variation onto the representatives of the homogenized strain field, which made formulation developed in this study relatively insensitive to the actual physical size of the cells and the actual boundary conditions among the adjacent cells.

3.3 Solution using a finite element method

By following a standard finite element approach and assuming an assembly of nodal displacement vectors, $\boldsymbol{\chi} = [\boldsymbol{\chi}^{(1)},\boldsymbol{\chi}^{(2)},...,\boldsymbol{\chi}^{(\mathrm{d})}]$ and a shape function $\boldsymbol{N} = \boldsymbol{N}(y)$ in Y, $\boldsymbol{\theta}(y)$ in Eq. (12) can be represented as

$$\boldsymbol{\theta} = \boldsymbol{N}(y)\boldsymbol{\chi}, \tag{19}$$

and we can have

$$\boldsymbol{\varphi} = \boldsymbol{B}_Y\boldsymbol{\chi} \text{ and } \delta\boldsymbol{\varepsilon}_1 = \boldsymbol{B}_Y\delta\boldsymbol{\xi}, \tag{20}$$

where

$$\boldsymbol{B}_Y = \boldsymbol{E}(\nabla)\boldsymbol{N}(y). \tag{21}$$

Substituting Eq. (20) into Eq. (11) gives

$$\int_Y \delta\xi^{\mathrm{T}}(\boldsymbol{B}_Y^{\mathrm{T}}\boldsymbol{D}^{\varepsilon}\boldsymbol{B}_Y)\boldsymbol{\chi}\mathrm{d}y + \int_Y \delta\boldsymbol{\xi}^{\mathrm{T}}\boldsymbol{B}_Y^{\mathrm{T}}\boldsymbol{D}^{\varepsilon}\mathrm{d}y = 0. \tag{22}$$

Equation (22) results in the following finite element equations:

$$\boldsymbol{K}_Y\boldsymbol{\chi}^{(i)} = \boldsymbol{F}_Y^{(i)} \quad (i = 1,2,...,\mathrm{d}), \tag{23}$$

where

$$\boldsymbol{K}_Y = \int_Y (\boldsymbol{B}_Y^{\mathrm{T}}\boldsymbol{D}^{\varepsilon}\boldsymbol{B}_Y)\mathrm{d}y, \tag{24}$$

and $\boldsymbol{F}_Y^{(i)}$ is the i-th column in $\boldsymbol{F}_Y$ and

$$\boldsymbol{F}_Y = -\int_Y \boldsymbol{B}_Y^{\mathrm{T}}\boldsymbol{D}^{\varepsilon}\mathrm{d}y. \tag{25}$$

Solving Eq. (23) for $\boldsymbol{\chi} = [\boldsymbol{\chi}^{(1)},\boldsymbol{\chi}^{(2)},...,\boldsymbol{\chi}^{(\mathrm{d})}]$ gives

$$\boldsymbol{\chi} = \boldsymbol{K}_Y^{-1}\boldsymbol{F}_Y = -\left(\int_Y \boldsymbol{B}_Y^{\mathrm{T}}\boldsymbol{D}^{\varepsilon}\boldsymbol{B}_Y\mathrm{d}y\right)^{-1}\left(\int_Y \boldsymbol{B}_Y^{\mathrm{T}}\boldsymbol{D}^{\varepsilon}\mathrm{d}y\right), \tag{26}$$

and then the homogenized material stiffness matrix can be obtained as

$$\boldsymbol{D}^H = \frac{1}{|Y|}\int_Y \boldsymbol{D}^{\varepsilon}(I + \boldsymbol{B}_Y\boldsymbol{\chi})\mathrm{d}y. \tag{27}$$

Note, it is interesting to compare Eq. (26) to the reduction equation in the Guyan reduction to see the similarities, as well as the similarity of the homogenization process with the Guyan Reduction (refer to Ref. [1]).

3.4 Characteristic modes

Notably, $\boldsymbol{\varphi}$ in Eq. (9) is a matrix constructed of d vectors (e.g., $\mathrm{d} = 6$ for three-dimensional solids), namely $\boldsymbol{\varphi} = [\boldsymbol{\varphi}^{(1)},\boldsymbol{\varphi}^{(2)},...,\boldsymbol{\varphi}_{\varphi}^{(\mathrm{d})}]$, where each $\boldsymbol{\varphi}^{(i)}$ is labeled a characteristic strain mode of the cellular structure corresponding to a forced unique strain field applied over the cellular Y domain, where $i = 1, 2, ..., \mathrm{d}$. In fact, Eq. (9) can be rewritten as

$$\boldsymbol{\varepsilon}_{\mathrm{v}} = \sum_{i=1}^{\mathrm{d}} \boldsymbol{\varphi}^{(i)}\varepsilon_{\mathrm{h}}^{(i)}, \tag{28}$$

where $\varepsilon_{\mathrm{h}}^{(1)} = \varepsilon_x$, $\varepsilon_{\mathrm{h}}^{(2)} = \varepsilon_y$, ..., $\varepsilon_{\mathrm{h}}^{(\mathrm{d})} = \gamma_{xy}$, and $\boldsymbol{\varepsilon}_{\mathrm{h}}$ can be rewritten using a strain coordinates system, $\boldsymbol{e}^{(i)}$ $(i = 1, 2,...,d)$, as

$$\boldsymbol{\varepsilon}_{\mathrm{h}} = \sum_{i=1}^{\mathrm{d}} \boldsymbol{e}^{(i)}\varepsilon_{\mathrm{h}}^{(i)}. \tag{29}$$

Here, for $d = 6$,

$$\boldsymbol{e}^{(1)} = \begin{Bmatrix} 1\\0\\0\\0\\0\\0 \end{Bmatrix},\ \boldsymbol{e}^{(2)} = \begin{Bmatrix} 0\\1\\0\\0\\0\\0 \end{Bmatrix},\ ...,\ \boldsymbol{e}^{(6)} = \begin{Bmatrix} 0\\0\\0\\0\\0\\1 \end{Bmatrix}. \tag{30}$$

By substituting Eqs. (28) and (29) into the second-row equation in Eq. (8), the equation for each *characteristic* strain mode $\boldsymbol{\varphi}^{(i)}$ can be obtained:

$$\int_Y \delta\varepsilon_{\mathrm{v}}^{\mathrm{T}}\boldsymbol{D}^{\varepsilon}\boldsymbol{\varphi}^{(i)}\mathrm{d}y + \int_Y \delta\varepsilon_{\mathrm{v}}^{\mathrm{T}}\boldsymbol{D}^{\varepsilon}\boldsymbol{e}^{(i)}\mathrm{d}y = 0 \quad (i = 1, 2,...,d). \tag{31}$$

Equation (31) describes the physical meaning of the *characteristic* strain mode $\boldsymbol{\varphi}^{(i)}$, which is the response to an applied uniform unit strain field $e^{(i)}$ in the cellular domain.

As shown in the second term of Eq. (31), each uniform strain $\boldsymbol{e}^{(i)}$ results in a stress field, described as a pre-stress applied in the cellular domain, such that

$$\boldsymbol{\sigma}_0^{(i)} = \boldsymbol{D}^{\varepsilon} e^{(i)} \ (i = 1,\ 2,...,d). \tag{32}$$

Therefore, Eq. (31) can also be rewritten as

$$\int_Y \delta\varepsilon_{\mathrm{v}}^{\mathrm{T}} \boldsymbol{D}^{\varepsilon} \boldsymbol{\varphi}^{(i)} \mathrm{d}y + \int_Y \delta\varepsilon_{\mathrm{v}}^{\mathrm{T}} \boldsymbol{\sigma}_0^{(i)} \mathrm{d}y = 0 \qquad (i = 1,\ 2,...,d). \tag{33}$$

The *characteristic deformation modes* of the cell can be obtained by solving Eq. (23) with the following loading condition:

$$\boldsymbol{F}_Y^{(i)} = -\int_Y \boldsymbol{B}_Y^{\mathrm{T}} \boldsymbol{D}^{\varepsilon} \boldsymbol{e}^{(i)} \mathrm{d}y \ (i = 1,\ 2,...,d). \tag{34}$$

Solving Eq. (23) with Eq. (34) for $\boldsymbol{\chi}^{(i)}$ results in

$$\boldsymbol{\chi}^{(i)} = -\left(\int_Y \boldsymbol{B}^{\mathrm{T}} \boldsymbol{D}^{\varepsilon} \boldsymbol{B} \mathrm{d}y\right)^{-1} \left(\int_Y \boldsymbol{B}^{\mathrm{T}} \boldsymbol{D}^{\varepsilon} \boldsymbol{e}^{(i)} \mathrm{d}y\right)$$

$$(i = 1,\ 2,...,d). \tag{35}$$

As a special example, for a two-dimensional solid problem, we have $\boldsymbol{\varepsilon}^{\mathrm{T}} = \{\varepsilon_x,\varepsilon_y,\gamma_{xy}\}^{\mathrm{T}}$, $\boldsymbol{u}^{\mathrm{T}} = \{u_x,u_y\}^{\mathrm{T}}$, $\boldsymbol{f}^{\mathrm{T}} = \{f_x,f_y\}^{\mathrm{T}}$, $\boldsymbol{t}^{\mathrm{T}} = \{t_x,t_y\}^{\mathrm{T}}$, and $\boldsymbol{\varepsilon}_h$ can be written as

$$\boldsymbol{\varepsilon}_{\mathrm{h}} = \sum_{i=1}^{3} \boldsymbol{e}^{(i)} \varepsilon_{\mathrm{h}}^{(i)}, \tag{36}$$

where

$$\boldsymbol{e}^{(1)} = \begin{Bmatrix} 1 \\ 0 \\ 0 \end{Bmatrix},\ \boldsymbol{e}^{(2)} = \begin{Bmatrix} 0 \\ 1 \\ 0 \end{Bmatrix},\ \boldsymbol{e}^{(3)} = \begin{Bmatrix} 0 \\ 0 \\ 1 \end{Bmatrix}. \tag{37}$$

Figure 8 illustrates the uniform unit strain fields in Eq. (37) applied in the two-dimensional cellular domain.

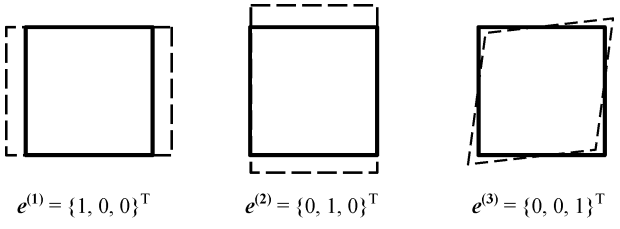

Fig. 8 Unit uniform strain field $e^{(i)}$ $(i = 1,2,3)$ applied in the 2-dimensional cellular domain

3.5 Extension to the stress-based method

The elastostatics problem in Eq. (1) can also be stated using the principle of virtual forces as

$$\int_{\Omega_\varepsilon} \delta\boldsymbol{\sigma}^{\mathrm{T}} \boldsymbol{A}^{\varepsilon} \boldsymbol{\sigma} \mathrm{d}\Omega = \int_{\Gamma_u} \delta\boldsymbol{p}^{\mathrm{T}} \overline{\boldsymbol{u}} \mathrm{d}\Gamma, \tag{38}$$

where $\boldsymbol{\sigma}$ ($\boldsymbol{\sigma}^{\mathrm{T}} = \{\sigma_x,\sigma_y,\sigma_z,\tau_{yz},\tau_{zx},\tau_{xy}\}^{\mathrm{T}}$ for 3-dimensional solids stands for the stress vector satisfying

$$\boldsymbol{E}(\nabla)^{\mathrm{T}} \sigma = \boldsymbol{f} \ \ (\text{in } \Omega_\varepsilon) \text{ and } \boldsymbol{E}(\eta)^{\mathrm{T}} \boldsymbol{\sigma} = \boldsymbol{t} \text{ on } \Gamma_u\ , \tag{39}$$

where $\boldsymbol{A}^{\varepsilon}$ is the material flexibility matrix; in general, we obtain

$$\boldsymbol{A}^{\varepsilon} = [\boldsymbol{D}^{\varepsilon}]^{-1}. \tag{40}$$

It is also assumed that $\delta\boldsymbol{\sigma}$ satisfies

$$\boldsymbol{E}(\nabla)^{\mathrm{T}} \delta\boldsymbol{\sigma} = 0 \text{ in } \boldsymbol{\Omega}_\varepsilon \text{ and } \boldsymbol{E}(\nu)^{\mathrm{T}} \delta\boldsymbol{\sigma} = \delta\boldsymbol{p} \text{ on } \Gamma_u\ . \tag{41}$$

Similar to the process described in Section 3.2, we assume

$$\boldsymbol{\sigma} = \boldsymbol{\sigma}_{\mathrm{h}} + \boldsymbol{\sigma}_{\mathrm{v}}, \tag{42}$$

where $\boldsymbol{\sigma}_{\mathrm{h}}$ stands for the homogenized stress field, $\boldsymbol{\sigma}_v$ is the stress variation from the homogenized stress field in the cellular domain; also, we assume

$$\boldsymbol{p} = \boldsymbol{p}_{\mathrm{h}} + \boldsymbol{p}_{\mathrm{v}}, \tag{43}$$

where $\boldsymbol{p}_{\mathrm{h}}$ stands for the boundary force corresponding to the homogenized stress field $\boldsymbol{\sigma}_{\mathrm{h}}$, $\boldsymbol{p}_{\mathrm{v}}$ stands for the boundary force corresponding to the stress variation $\boldsymbol{\sigma}_{\mathrm{v}}$. Equation (38) can be then rewritten as

$$\begin{cases} \displaystyle\int_{\Omega_\varepsilon} \delta\boldsymbol{\sigma}_h^{\mathrm{T}} \boldsymbol{A}^{\varepsilon} (\boldsymbol{\sigma}_h + \boldsymbol{\sigma}_v) \mathrm{d}\Omega = \int_{\Gamma_u} \delta(\boldsymbol{p}_h + \boldsymbol{p}_v)^{\mathrm{T}} \overline{\boldsymbol{u}} \mathrm{d}\Gamma \\ \displaystyle\int_Y \delta\boldsymbol{\sigma}_v^{\mathrm{T}} \boldsymbol{A}^{\varepsilon} (\boldsymbol{\sigma}_h + \boldsymbol{\sigma}_v) \mathrm{d}y = 0 \qquad \text{for } \forall Y \in \Omega \end{cases}. \tag{44}$$

Similar to the process in Section 3.2, we assume a set of stress modes $\boldsymbol{z} = [\boldsymbol{z}^{(1)},\boldsymbol{z}^{(2)},...,\boldsymbol{z}^{(\mathrm{d})}]$ and

$$\boldsymbol{\sigma}_{\mathrm{h}} = \sum_{i=1}^{\mathrm{d}} \boldsymbol{e}_1^{(i)} \boldsymbol{\sigma}_h^{(i)} \text{ and } \boldsymbol{\sigma}_{\mathrm{v}} = \sum_{i=1}^{\mathrm{d}} \boldsymbol{z}^{(i)} \boldsymbol{\sigma}_{\mathrm{h}}^{(i)}. \tag{45}$$

Substituting Eq. (45) into the second-row equation in Eq. (44) results in

$$\int_Y \delta\boldsymbol{\sigma}_{\mathrm{v}}^{\mathrm{T}} \boldsymbol{A}^{\varepsilon} \boldsymbol{z}^{(i)} \mathrm{d}y + \int_Y \delta\boldsymbol{\sigma}_{\mathrm{v}}^{\mathrm{T}} \boldsymbol{A}^{\varepsilon} \boldsymbol{e}^{(i)} \mathrm{d}y = 0 \quad (i = 1,\ 2,...,d), \tag{46}$$

then $\boldsymbol{z}^{(i)}$ $(i = 1,2,...,d)$ can be obtained by solving Eq. (46) with the properly defined (periodic) boundary conditions, and then the first-row equation in Eq. (44) becomes

$$\int_\Omega \delta\boldsymbol{\sigma}_{\mathrm{h}}^{\mathrm{T}} \boldsymbol{A}^{H} \boldsymbol{\sigma}_{\mathrm{h}} \mathrm{d}\Omega = \int_{\Gamma_u} \delta\boldsymbol{p}_{\mathrm{h}}^{\mathrm{T}} \overline{\boldsymbol{u}}^{H} \mathrm{d}\Gamma, \tag{47}$$

where

$$\boldsymbol{A}^H = \frac{1}{|Y|}\int_Y \boldsymbol{A}^{\varepsilon}(\boldsymbol{I}+\boldsymbol{z}_1)\mathrm{d}y, \tag{48}$$

$$\overline{\boldsymbol{u}}^H = \frac{1}{|L|}\int_{\Gamma_{uY}} (\boldsymbol{I}+\boldsymbol{\omega})^{\mathrm{T}}\overline{\boldsymbol{u}}\mathrm{d}s, \tag{49}$$

such that

$$\boldsymbol{E}(\nu)^{\mathrm{T}}\boldsymbol{z} = \boldsymbol{\omega} \text{ on } \Gamma_{uY} \text{ and } \Gamma_{uY} = \Gamma_u \cap Y. \tag{50}$$

Note, it is not necessary for the stress-based homogenization process to produce the same effective material properties as the strain-based homogenization process. In fact, based on the principle of virtual displacements and principle of virtual forces, the strain-based homogenization process may provide an upper boundary for the effective material properties; the stress-based homogenization process provides a lower bound for the effective material properties.

As a special example, for a two-dimensional solids problem, we have $\boldsymbol{\sigma}^{\mathrm{T}} = \{\sigma_x,\sigma_y,\tau_{xy}\}^{\mathrm{T}}$, and $\boldsymbol{\sigma}_{\mathrm{h}}$ becomes

$$\boldsymbol{\sigma}_{\mathrm{h}} = \sum_{i=1}^{3} \boldsymbol{e}^{(i)}\sigma_{\mathrm{h}}^{(i)}. \tag{51}$$

Figure 9 illustrates the uniform unit stress fields in Eq. (46) applied in the two-dimensional cellular domain.

Note that in Eq. (51), $\sigma_h^{(1)} = \sigma_x$, $\sigma_h^{(2)} = \sigma_y$, $\sigma_h^{(3)} = \tau_{xy}$ is assumed.

3.6 Extension to the discrete systems

With the above understanding, the extension to discrete systems can easily be performed by first converting the applied unit stress field into concentrated forces and applying them to the proper nodes of the cellular structure; second, one must calculate the displacements at the properly selected nodes to approximate the strain in the cellular domain and use the obtained information to approximate the effective material properties. As an example, Fig. 10 uses a two-dimensional version of the NPR material shown in Fig. 5 to illustrate the loading conditions and boundary conditions for the homogenization of a 2D NPR cell structure.

In Fig. 10, the vertical direction is set as the x-direction, and the horizontal direction is set as the y-direction. As shown in Fig. 10, there are three analysis cases corresponding to the three characteristic modes in the homogenization problem. Each loading case corresponds to a unit stress field with an amplitude equal to the facing area multiplied by the unit stress, which is 1. The boundary conditions were determined by the periodicity consideration as well as the symmetry of the cell structure and the connectivity to the adjacent cells.

As shown in the left figure in Fig. 10, a concentrated force P_1 was applied at Point F, which represents the tension stress on the top of the cell. Here, boundary condition E (1, 1, 1) indicates that Node E is fixed along all of the directions, including the x- and y-directions as well as the deformation angle. Additionally, A (0, 0, 1) indicates that only the deformation angle is fixed at Node A, and this is the same for Node C.

As shown in the middle figure in Fig. 10, two concentrated forces with equal amplitudes P_2 were applied at Points A and C in opposite directions, representing the tension stress on the two sides of the cell. Here, the boundary conditions were the same as in the left figure.

The right figure in Fig. 10 illustrates a shear force applied on the cellular cell, for which $C = A$ indicates the periodicity boundary conditions required to be applied at Nodes A and C, and F (1, 1, p) and E (1, 1, p) indicate the periodicity boundary conditions for the deformation angle at Nodes F and E.

Note that the boundary conditions must be considered case by case for the typical cell configuration, structural symmetry, and connectivity with the adjacent cells in addition to the periodic arrangement of the cells in the global domain.

3.7 Strain and stress recoveries

After the global analysis, the homogenized strain ε_{h} is obtained, and it is easy to recover the local strain in the

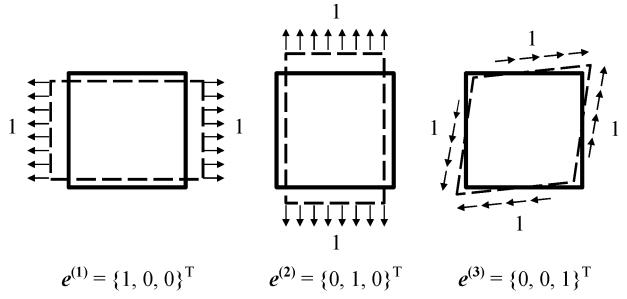

Fig. 9 Unit uniform stress field $e^{(i)}$ $(i = 1,2,3)$ applied on the 2-dimensional cellular domain

cellular domain as

$$\varepsilon = \varepsilon_{\mathrm{h}} + \varepsilon_{\mathrm{v}} = (\boldsymbol{I} + \boldsymbol{\varphi})\varepsilon_{\mathrm{h}}, \tag{52}$$

and therefore, the local stress is calculated as

$$\boldsymbol{\sigma} = \boldsymbol{D}^{\varepsilon}\boldsymbol{\varepsilon} = \boldsymbol{D}^{\varepsilon}(\boldsymbol{I} + \boldsymbol{\varphi})\varepsilon_{\mathrm{h}}. \tag{53}$$

Since

$$\boldsymbol{\varepsilon}_h = (\mathbf{D}^H)^{-1}\boldsymbol{\sigma}_h, \tag{54}$$

submit Eq. (54) into Eq. (53) obtains

$$\boldsymbol{\sigma} = \boldsymbol{z}_1\boldsymbol{\sigma}_{\mathrm{h}}, \tag{55}$$

here

$$\boldsymbol{z}_1 = \boldsymbol{D}^{\varepsilon}(\boldsymbol{I} + \boldsymbol{\varphi})(\boldsymbol{D}^H)^{-1}. \tag{56}$$

From Eqs. (42) and (45), we have

$$\boldsymbol{\sigma} = \boldsymbol{\sigma}_{\mathrm{v}} + \boldsymbol{\sigma}_{\mathrm{h}} = (\boldsymbol{I} + \boldsymbol{z})\boldsymbol{\sigma}_{\mathrm{h}}. \tag{57}$$

Comparing Eq. (55) with Eq. (57) we have

$$\boldsymbol{z} = \boldsymbol{z}_1 - \boldsymbol{I}, \tag{58}$$

where, z is the characteristic stress modes.

Note that when the homogenized strain and stress $\boldsymbol{\varepsilon}_{\mathrm{h}}$ and $\boldsymbol{\sigma}_{\mathrm{h}}$ are known, the strain mode $\boldsymbol{\varphi}$ and stress mode z can be used to recover the local strain and stress by using Eqs. (52) and (57). These local strain and stress modes can be then used to determine the potential failures and failure modes of the MAC material or to predict the strength (or the plastic deformation limit) of the MAC material. Furthermore, the failure modes can be utilized to determine the critical loads and to further improve the architecture design of the MAC material.

4 Material properties and characteristic modes of NPR materials

4.1 Material properties

Figure 10 illustrated three analytical cases with the loading and boundary conditions for the homogenization of a 2D NPR cell structure. In the following analyses, we considered the homogenization problem of the 3D NPR material shown in Fig. 5. Owing to the symmetry of the cell structure, we considered only a quarter of the cell structure, which results in a two-dimensional analysis problem as shown in Fig. 11; meanwhile, Fig. 11 illustrates the problem setup for the first mode under a unit stress $e^{(1)} = \{1,0,0,0,0,0\}^{\mathrm{T}}$. Here, in Fig. 11, the concentrated force P_1 should be a quarter of the total force (unit stress multiplied by the top area of the cell) applied on the top of the cell. The boundary conditions were determined by considering the periodic conditions as well as the connectivity among the adjacent cells as discussed in Section 3.6.

The analytical problem shown in Fig. 11 can be analytically solved using the assumption of the Euler-Bernoulli beam for the bending along with the tension of all of the members. As a result, we obtained the analytical solution for Δ_1 and Δ_2 as functions of P_1 as follows:

$$\begin{cases} \Delta_1 = \dfrac{(g_{11}^1 + g_{11}^2)(g_{22}^1 + g_{22}^2) - (g_{12}^1 + g_{12}^2)^2}{g_{11}^1 + g_{11}^2} P_1 \\ \Delta_2 = \dfrac{g_{11}^2 g_{12}^1 - g_{12}^2 g_{11}^1}{g_{11}^1 + g_{11}^2} P_1 \end{cases}, \tag{59}$$

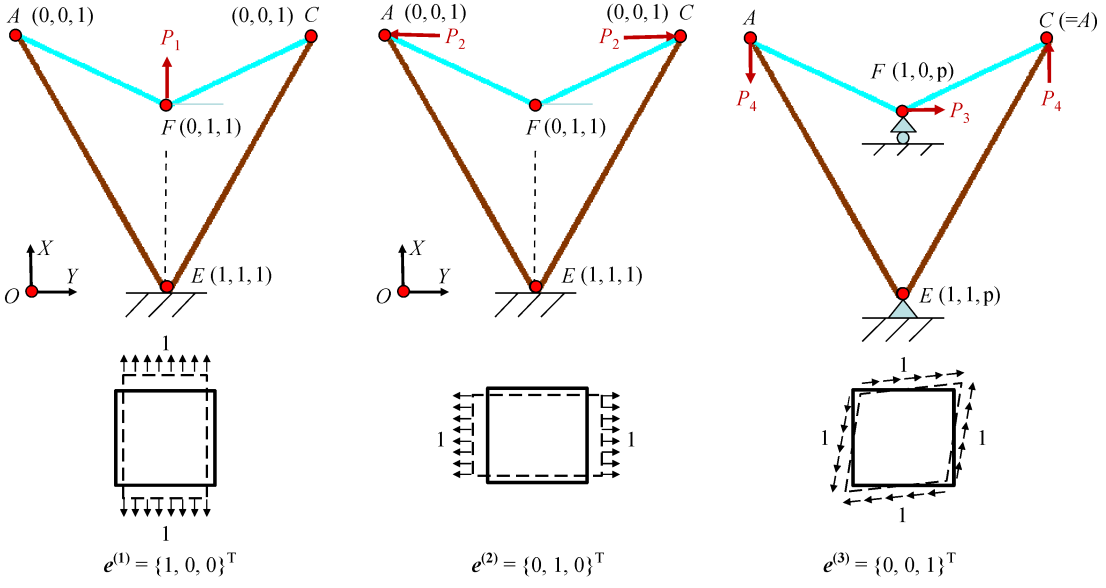

Fig. 10 Loading and boundary conditions for the homogenization of a 2D NPR cell structure

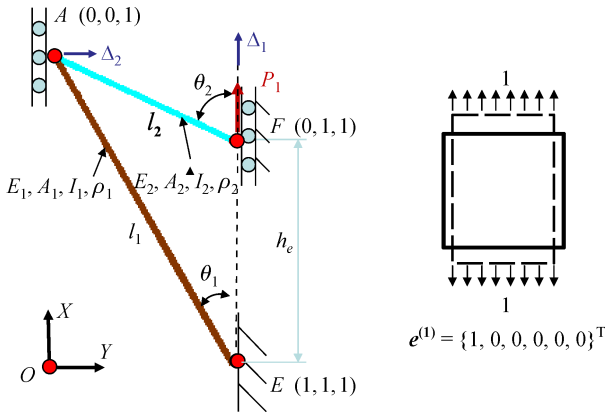

Fig. 11 Analysis model for characteristic mode 1

where

$$\begin{cases} g_{11}^1 = a_1\sin^2\theta_1 + b_1\cos^2\theta_1 \\ g_{12}^1 = (a_1 - b_1)\sin\theta_1\cos\theta_1 \\ g_{22}^1 = a_1\cos^2\theta_1 + b_1\sin^2\theta_1 \end{cases}, \tag{60}$$

$$\begin{cases} g_{11}^2 = a_2\sin^2\theta_2 + b_2\cos^2\theta_2 \\ g_{12}^2 = (a_2 - b_2)\sin\theta_2\cos\theta_2 \\ g_{22}^2 = a_2\cos^2\theta_2 + b_2\sin^2\theta_2 \end{cases},$$

$$a_1 = \frac{l_1}{E_1A_1},\ b_1 = \frac{l_1^3}{12E_1I_1},\ a_2 = \frac{l_2}{E_2A_2},\ b_2 = \frac{l_2^3}{12E_2I_2}. \tag{61}$$

In the above formulation, there are only 3 independent design variables among θ_1, θ_2, l_1, and l_2, and the following relationship exists

$$l_1\sin\theta_1 = l_2\sin\theta_2. \tag{62}$$

The mass density can be obtained as

$$\rho^H = 4(\rho_1 l_1 A_1 + \rho_2 l_2 A_2)/V_e, \tag{63}$$

where V_e is the total volume of the cell.

Based on the above analysis, the corresponding strains along the x and y directions were obtained. Here, $\varepsilon_X = \Delta_1/h_e$ and $\varepsilon_Y = \Delta_2/(l_1\sin\theta_1)$. Figure 12 illustrates the effective Young's modulus (GPa) as a function of two design variables, θ_1 and θ_2. Here, the horizontal axis was θ_1 and the vertical axis was the difference angle between θ_2 and θ_1. For this typical setup, the material became stiffer when θ_1 became small and the difference between θ_2 and θ_1 became small; the effective Young's modulus (in black) varied from 1 to 50 GPa in the parameter range considered. Figure 12 also shows the density contour (in red) as a

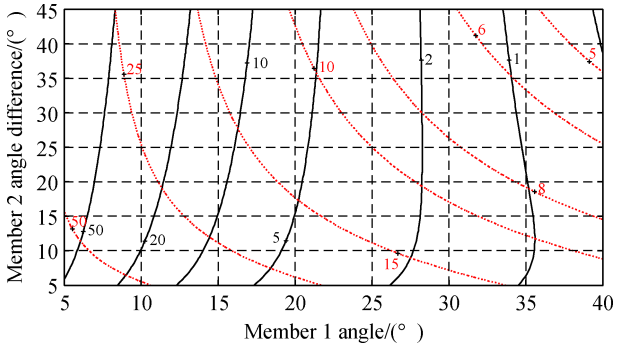

Fig. 12 Effective Young's modulus (in black and GPa) for Mode 1

percentage with respect to the design variables. It is seen that the density also increased when θ_1 became small and the angle difference became small; meanwhile, from the map, the optimal designs can be obtained for the given densities. For example, a 50 GPa design can be obtained at a material density of 25% when θ_1 is approximately 8° and θ_2 is 53°. Figure 13 illustrates the effective Poisson's ratio (as a percentage) obtained from the analysis. The Poisson's ratio reached the most negative number (less than −0.6) when θ_1 was within 10°−15°, θ_2 was within 20°−30°, and the material density was near 25%. Notably, the analysis results depended on the other parameters used for the cell element; however, studying the actual material properties was not the purpose of this study.

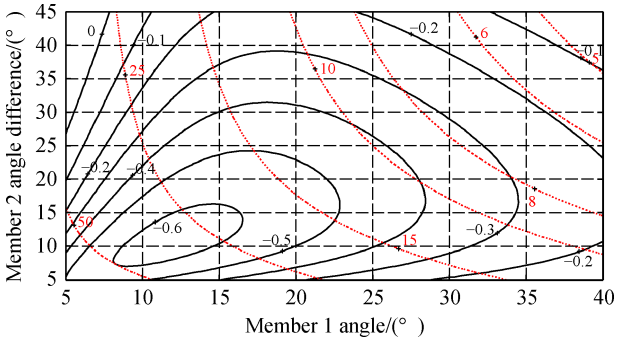

Fig. 13 Effective Poisson's ratio (in black and 100%) for Mode 1

Figure 14 illustrates the problem setup for the second mode under a unit stress $\boldsymbol{e}^{(2)} = \{0,1,0,0,0,0\}^{\mathrm{T}}$. Owing to the symmetry of the cell structure, we considered only a quarter of the cell structure and the two-dimensional analysis problem shown in Fig. 14. Here, the concentrated force P_2 should be the total force because of the unit stress applied on the side of the cell.

The analytical problem shown in Fig. 14 can be analytically solved with the same assumptions as the first case. As a result, for Mode 2, we have

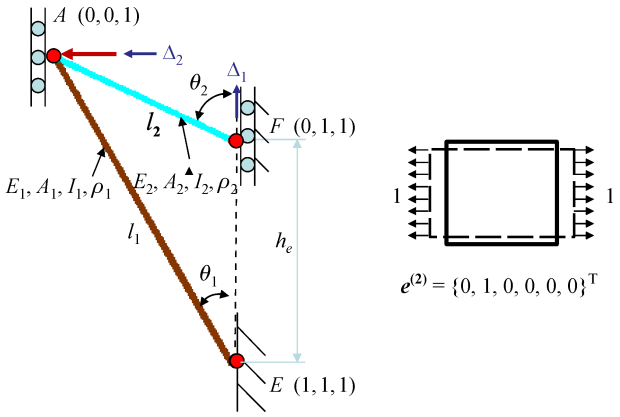

Fig. 14 Analysis model for characteristic Mode 2

$$\begin{cases} \Delta_1 = \dfrac{g_{11}^2 g_{12}^1 - g_{12}^2 g_{11}^1}{g_{11}^1 + g_{11}^2} P_2 \\ \Delta_2 = \dfrac{g_{11}^1 g_{12}^2}{g_{11}^1 + g_{11}^2} P_2 \end{cases}. \tag{64}$$

Figure 15 illustrates the effective Young's modulus (GPa) (in black) as a function of the two design variables θ_1 and θ_2. For this typical setup, the material became stiffer when θ_1 became larger and the difference between θ_2 and θ_1 became larger; the effective Young's modulus varied from 0.5 to 20 GPa in the parameter range considered. Figure 16 illustrates the effective Poisson's ratio (100%) obtained from the analysis. The Poisson's ratio reached the most negative number (less than −2.0) when θ_1 approached 40φ and θ_2 was within 70φ−80°.

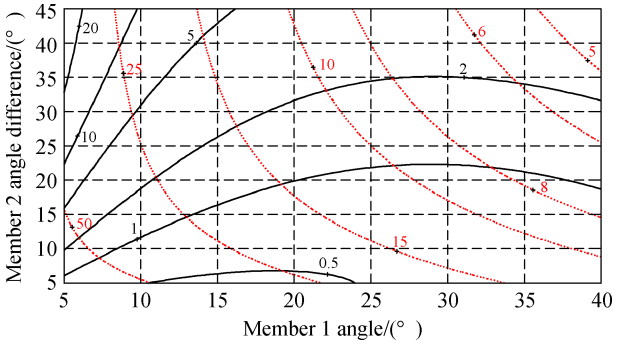

Fig. 15 Effective Young's modulus (in black and GPa) for Mode 2

Note that the shear mode shown on the right in Fig. 10 and the other two shear modes in the three-dimensional problem could have been considered but were omitted in this study.

4.2 Characteristic modes

Figure 8 illustrates the uniform unit strain fields in Eq. (37) applied in the two-dimensional cellular domain. As an example, Fig. 17 illustrates the characteristic deformation modes for the unit cell of a two-dimensional NPR material obtained using the homogenization process presented in this study. Here, the top left is the deformation shape of the first characteristic mode corresponding to a unit strain field $\boldsymbol{e}^{(1)} = \{1,0,0\}$, the top middle is the deformation shape of the second characteristic mode corresponding to a unit strain field $\boldsymbol{e}^{(2)} = \{0,1,0\}$, and the top right is the deformation shape of the third characteristic mode corresponding to a unit strain field $\boldsymbol{e}^{(3)} = \{0,0,1\}$.

Fig. 16 Effective Poisson's ratio (in black and 100%) for Mode 2

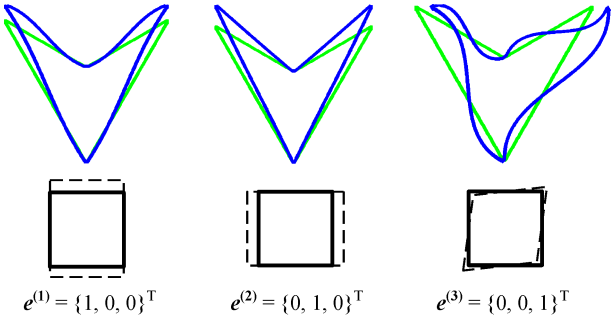

Fig. 17 Unit uniform strain field applied in the 2-dimesional cellular domain (top left: Characteristic Mode 1, top middle: Characteristic Mode 2, top right: Characteristic Mode 3)

Figures 18−20 further illustrate the strain distributions in the above characteristic modes. Figure 18 is the strain distribution in the first characteristic mode, Fig. 19 in the second characteristic mode, and Fig. 20 in the third characteristic mode.

Note, using Eqs. (56) and (58), the stress distributions in the characteristic modes can also be obtained, but these were omitted in this study.

5 Material properties of BTR materials

To estimate the effective material properties of BTR materials, a strain-based homogenization process was used. Figure 21 illustrates the three major characteristic

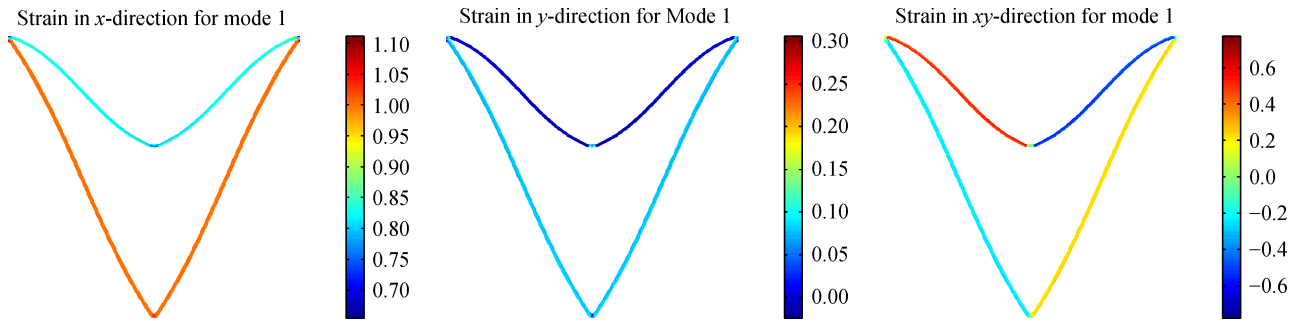

Fig. 18 Strain distribution of characteristic Mode 1 (left: ε_x, middle: ε_y, right: γ_{xy})

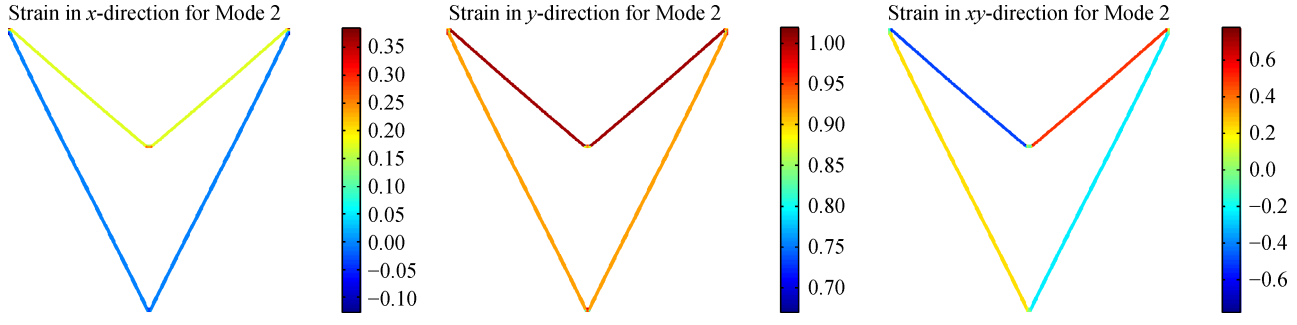

Fig. 19 Strain distribution of characteristic Mode 2 (left: ε_x, middle: ε_y, right: γ_{xy})

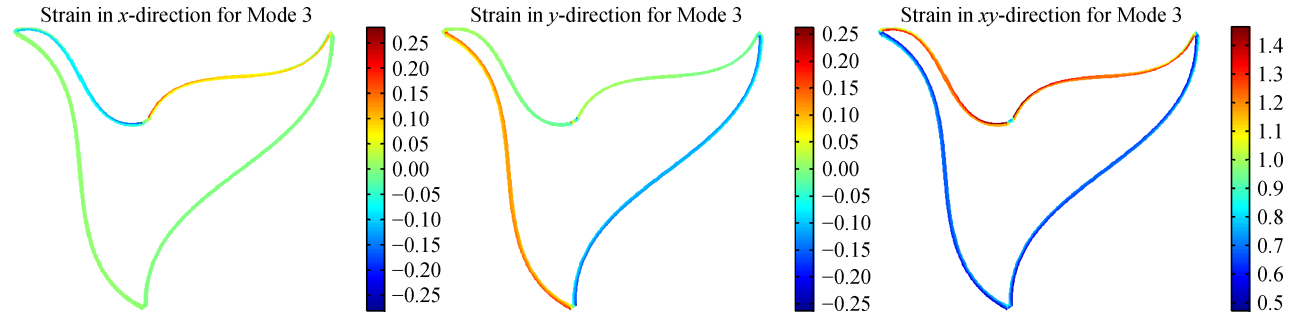

Fig. 20 Strain distribution of characteristic Mode 3 (left: ε_x, middle: ε_y, right: γ_{xy})

modes considered in this study. Note that the two-dimensional figures shown in Fig. 21 actually represent three-dimensional structures. Additionally, note that because a major advantage of BTR material is its high out-of-plane bending stiffness and out-of-plane bending strength, the effective bending stiffness was considered (Fig. 21(c)) instead of the shear modulus.

From Fig. 21(a), the homogenized in-plane tension modulus $E^H_{\text{in-plane}}$ can be obtained as

$$E^H_{\text{in-plane}} = \frac{2t_1}{h_2+2t_1}E_1 + \frac{2l_1^2A_3}{(h_2+2t_1)(l_1^2+h_2^2)^{\frac{3}{2}}}E_3. \quad (65)$$

From Fig. 21(b), the homogenized out-of-plane compression modulus $E^H_{\text{out-plane}}$ can be obtained as

$$E^H_{\text{out-plane}} = \frac{1}{l_1^2}\left(\frac{(h_2+2t_1)E_1E_2}{h_2E_1+2t_1E_2}A_2 + \frac{4(h_2+2t_1)h_2^3A_3}{l_1(l_1^2+h_2^2)^{\frac{3}{2}}}E_3\right). \quad (66)$$

From Fig. 21(c), the homogenized (unit) bending stiffness $(EI)^H_{\text{bending}}$ can be obtained as

$$(EI)^H_{\text{bending}} = \frac{1}{12}E_1[(h_2+2t_1)^3-(h_2)^3]. \quad (67)$$

The effective mass density ρ^H can be obtained as

$$\rho^H = \frac{2t_1}{h_2+2t_1}\rho_1 + \frac{A_2}{l_1^2}\rho_2 + \frac{4\sqrt{l_1^2+h_2^2}A_3}{l_1^2h_2}\rho_3. \quad (68)$$

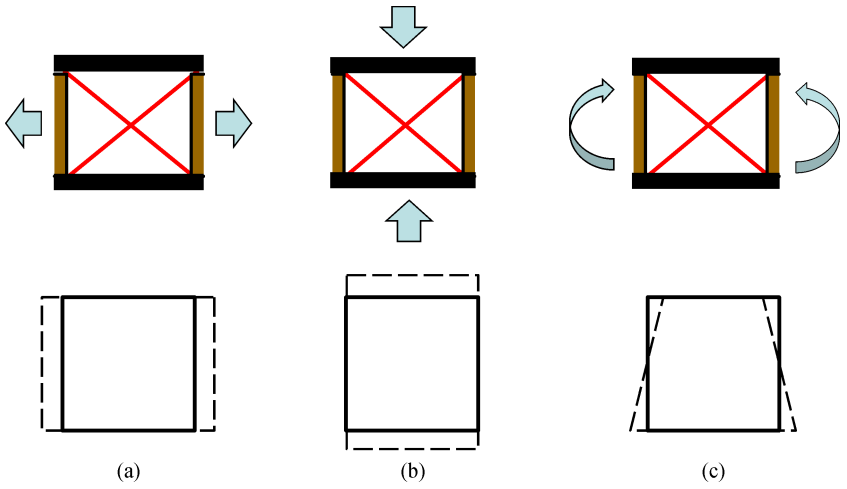

Fig. 21 Strain modes of BTR cell. (a) In-plane tension; (b) out-plane compression; (c) pure bending

Figures 22–24 illustrate example results obtained from the above formulations for a typical design case. Here, only two design variables, the stuffer height h_2 and the sheet thickness t_1, were varied for the parametric studies. Note that all the results in Figs. 22–24 were normalized with the initial values $t_1 = 1$ mm and $h_2 = 15$ mm.

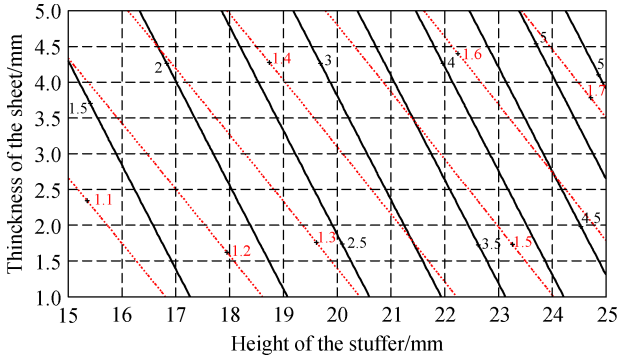

Fig. 22 Normalized bending stiffness-normalized area density map

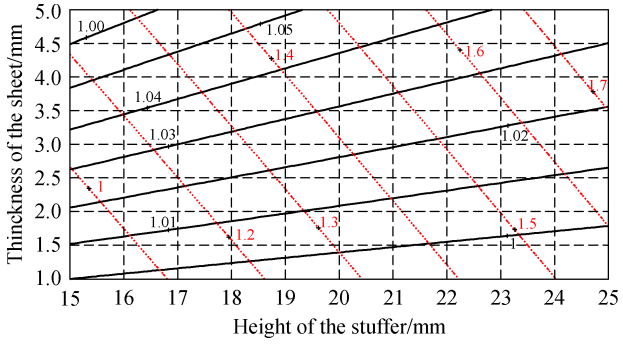

Fig. 23 Normalized in-plane modulus-normalized area density map

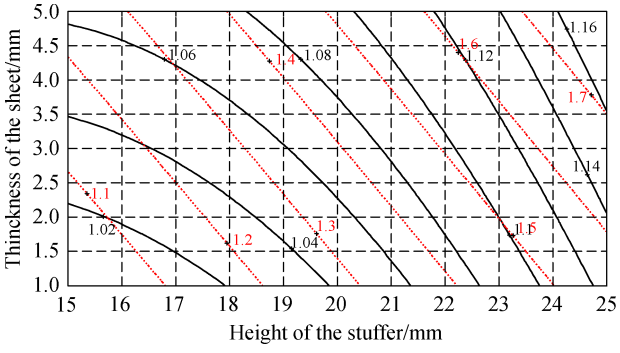

Fig. 24 Normalized out-of-plane compression modulus-normalized area density map

Figure 22 shows the normalized bending stiffness with the normalized area density. The bending stiffness increased by increasing either design parameter, but an increase in the stuffer height was more effective than increasing the sheet thickness. This map was useful for selecting a proper design. For example, by selecting $t_1 = 1.5$ mm and $h_2 = 21.6$ mm, we could increase the bending stiffness by 3 times while only increasing the area density by 1.4 times.

Figure 23 shows the normalized in-plane modulus with the normalized area density. The in-plane modulus was insensitive to the design changes in this case. Figure 24 further shows the normalized out-of-plane compression modulus with the normalized area density. In this case, the out-of-plane modulus decreased when the stuffer height was increased, but it was less sensitive to design changes in the sheet thickness. Note that the analysis results also depended on other parameters used for the cell element; however, studying the actual material properties was not the purpose of this study.

6 Conclusions

MAC material is defined as a class of engineered materials having configurable cells of relatively large size. MAC materials can be architecturally designed to achieve various desired material properties. Two types of novel MAC materials, negative Poisson's ratio material and biomimetic tendon reinforced material, were introduced in this study. To estimate the effective material properties and to optimally design such materials, a set of suitable homogenization methods was developed to provide an effective means for the multiscale modeling of MAC materials.

A mechanics-based homogenization approach was presented, resulting in two versions of the method: strain-based homogenization and stress-based homogenization. The strain-based homogenization process was obtained based on the principle of virtual displacements, and the stress-based homogenization process was obtained based on the principle of virtual forces. Strain-based homogenization separates the strain field into a homogenized strain field and a strain variation field superposed on the homogenized strain field. The stress-based homogenization separates the stress field into a homogenized stress field and a stress variation field. The principle of virtual displacements (principle of virtual forces) for the relationship between the strain (stress) variation field and the homogenized strain (stress) field was then used to condense the strain (stress) variation field to the homogenized strain (stress) field, and the homogenization processes became coordinate reductions similar to a Guyan reduction.

The new derivation in this study provided improved engineering insight and enhanced physical understanding for dealing with boundary conditions, internal forces, and other issues in the homogenization modeling processes. The stress-based homogenization process can be extended easily to handle discrete systems, providing a bridge between discrete and continuum systems. The mode analysis and the recovery process presented in this study are useful tools for failure mode prediction, failure mode management, and the design optimization of architectured materials.

This new method provides an alternative means to further improve the accuracy and efficiency of multi-scale analysis problems. The formulations developed in this study included calculating the effective (homogenized) mass density, which can be directly used for dynamics analyses of structures based on MAC materials. It was noted that by iterating the analysis process, this method can also be extended to solving nonlinear problems, which will be discussed in a separate study. Furthermore, it can be easily extended to handle other various mechanical simulation and design problems. The newly derived method was utilized to obtain the effective material properties of the novel architectured cellular materials discussed in this study.

Acknowledgements This work was supported by MKP Structural Design Associates, Inc., a corporation in Ann Arbor, Michigan, USA.

References

1. Ma Z D. Homogenization method for designing novel architectured cellular materials. In: Proceedings of VII ECCOMAS Congress. Crete Island, 2016
2. Fleck N A, Deshpande V S, Ashby M F. Micro-architectured materials: Past, present and future. Proceedings of the Royal Society A: Mathematical, Physical and Engineering Sciences, 2010, 466 (2121): 2495–2516
3. Wang Y Q, Chen F F, Wang M Y. Concurrent design with connectable graded microstructures. Computer Methods in Applied Mechanics and Engineering, 2017, 317: 84–101
4. Alexandersen J, Lazarov B S. Topology optimization of manufacturable microstructural details without length scale separation using a spectral coarse basis preconditioner. Computer Methods in Applied Mechanics and Engineering, 2015, 290: 156–182
5. Ma Z D. US Patent, 7910193, 2011-03-22
6. Ma Z D. US Patent, 7563497, 2009-07-21
7. Ma Z D, Cui Y. US Patent, 20110117309, 2011-05-19
8. Weinan E, Engquist B, Li X, et al.The heterogeneous multiscale methods: A review. Communications in Computational Physics, 2004, 2(3): 367–450
9. Kanouté P, Boso D P, Chaboche J L, et al.Multiscale methods for composites: A review. Archives of Computational Methods in Engineering, 2009, 16(1): 31–75
10. Nguyen V P, Stroeven M, Sluys L J. Multiscale continuous and discontinuous modeling of heterogeneous materials: A review on recent developments. Journal of Multiscale Modelling, 2011, 3(4): 229–270
11. Sanchez-Palencia E. Non-Homogenous Media and Vibration Theory. Berlin: Springer, 1980
12. Benssousan A, Lions J L, Papanicoulau G. Asymptotic analysis for periodic structures. Amsterdam: Elsevier, 1978
13. Cioranescu D, Paulin J S J. Homogenization in open sets with holes. Journal of Mathematical Analysis and Applications, 1979, 71(2): 590–607
14. Bendsøe M P, Kikuchi N. Generating optimal topologies in structural design using homogenization method. Computer Methods in Applied Mechanics and Engineering, 1988, 71(2): 197–224
15. Ma Z D, Kikuchi N, Cheng H C. Topological design for vibrating structures. Computer Methods in Applied Mechanics and Engineering, 1995, 121(1-4): 259–280
16. Arabnejad S, Pasini D. Mechanical properties of lattice materials via asymptotic homogenization and comparison with alternative homogenization methods. International Journal of Mechanical Sciences, 2013, 77: 249–262
17. Terada K, Kikuchi N. A class of general algorithms for multi-scale analyses of heterogeneous media. Computer Methods in Applied

Mechanics and Engineering, 2001, 190(40–41): 5427–5464
18. Abdulle A, Bai Y. Reduced-order modelling numerical homogenization. Philosophical Transactions. Series A, Mathematical, Physical, and Engineering Sciences, 2014, 372(2021): 20130388
19. Cong Y, Nezamabadi S, Zahrouni H, et al.Multiscale computational homogenization of heterogeneous shells at small strains with extensions to finite displacements and buckling. International Journal for Numerical Methods in Engineering, 2015, 104(4): 235–259 doi:10.1002/nme.4927
20. Dos Reis F, Ganghoffer J F. Discrete homogenization of architectured materials: Implementation of the method in a simulation tool for the systematic prediction of their effective elastic properties. Technische Mechanik, 2010, 30: 85–109
21. Guyan R J. Reduction of stiffness and mass matrices. AIAA Journal, 1965, 3(2): 380
22. Lakes R S. Negative Poisson's ratio materials. Science, 1987, 238 (4826): 551
23. Zhou G, Ma Z D, Li G, et al.Design optimization of a novel NPR crash box based on multi-objective genetic algorithm. Structural and Multidisciplinary Optimization, 2016, 54(3): 673–684
24. Ma Z D, Liu Y Y, Liu X M, et al.US Patent/Chinese patent, 8544515/201110401962.4, 2013-10-01
25. Ma Z D. US Patent, 9376796, 2016-06-18
26. Ma Z D, Liu Y Y. US Patent, 20110029063, 2011-02-03
27. Ma Z D, Wang H, Cui Y, et al.Designing an innovative composite armor system for affordable ballistic protection. In: Proceedings of 25th Army Science Conference. Orlando, 2006
28. Jiang D, Liu Y, Qi C, et al.Innovative Composite Structure Design for Blast Protection. SAE Technical Paper 2007-01-0483. 2007